Supplemental Experimental Procedures

Compounds and reagents

BSB (Dojindo) (Skovronsky et al., 2002), FSB (Dojindo) (Higuchi et al., 2005; Maeda et al., 2007), PIB (ABX) (Klunk et al., 2004), FDDNP (ABX) (Small et al., 2006), dimethylamino-styryl-benzothiazole (Sigma-Aldrich), thioflavin-T (Sigma-Aldrich) and thioflavin-S (Waldeck) were commercially provided. BF-227 (Kudo et al., 2007), BF-158 (Okamura et al., 2005), THK523 (Fodero-Tavoletti et al., 2011) and BF-189 (N-methyl-4-[6-(quinolin-2-yl)hexa-1,3,5-trienyl]aniline) were also custom-made (Tanabe R&D Service). Other amyloid or β-sheet binding compounds, including PBB5 (Sigma-Aldrich), BTA-1 (Sigma-Aldrich) (Klunk et al., 2004), BF-170 (Sigma-Aldrich) (Okamura et al., 2005) and curcumin (Sigma-Aldrich) (Yang et al., 2005), and potential amyloid ligands, including cyanines, pyridines, pyridiniums, benzothiazoles, oxazines, thionins and polyphenols, were purchased for the initial screening. DMSO (Sigma-Aldrich) and other chemical reagents were commercially purchased.

In vitro fluorometric binding assays

Aβ40 fibrils were generated by incubating synthetic peptide (Peptide Institute) for 72 hr at 37°C. Recombinant T40 proteins were self-assembled into filaments by incubation with 0.1 mg/ml heparin for 72 hr at 37°C. Synthetic Aβ40 peptides (Peptide Institute) were dissolved in phosphate-buffered saline (PBS; pH 7.4) to a final concentration of 100 μM, and incubated for 72 hr at 37°C. The resultant solution was diluted to 50 μM, and an equal volume of fluorescent compounds (0 – 0.5 mM in PBS containing < 1% DMSO) was added to the solution. Following the reaction for 1 hr at 37°C, the samples were assayed by microplate spectrometer (Safire; Tecan). Human T40 (longest tau

isoform consisting of 441 amino acid residues) was expressed in E. coli DE3, purified and dialyzed against 30 mM Tris-HCl buffer (pH 7.5). Recombinant tau proteins (1 mg/ml) separated by reverse-phase HPLC were self-polymerized for 72 hr at 37°C in 30 mM Tris-HCl buffer with heparin (0.1 mg/ml). The tau fibrils (1 μM) were then reacted with an equal volume of β-sheet ligands, and assayed as in the analysis for binding to Aβ40. Saturation plots and parametric estimations for the fluorometric data were performed using Prism software (GraphPad).

Postmortem brain tissues

Postmortem human brains were obtained from autopsies carried out in the Center for Neurodegenerative Disease Research at the University of Pennsylvania Perelman School of Medicine on patients with AD, Pick's disease, PSP, CBD and FTLD characterized by TDP-43 inclusions. Tissues were fixed in 10% neutral buffered formalin and embedded in paraffin blocks. Brains were also collected from mice and fixed in 4% paraformaldehyde in phosphate buffer. Tissue samples were sliced in a cryostat (HM560; Carl Zeiss) after cryoprotection with 30% sucrose in phosphate buffer.

***Ex vivo* multiphoton imaging**

PS19 mice were intravenously injected with 1 mg/kg PBB2 and PBB4 dissolved in 100 μl of saline containing 20% DMSO, and their brains and spinal cords were dissected 60 min after tracer administration. Unsliced spinal cord samples were then examined by 2-photon fluorescence generated with 800-nm excitation from a pulsed laser (Mai Tai; Spectra-Physics) mounted on a multiphoton imaging system (TCS SP5 MP; Leica

Microsystems). Detection wavelength was 540 – 590 nm.

In vivo multiphoton imaging

WT and PS19 mice at 12 months of age were anesthetized with 1.5% (v/v) isoflurane and underwent laminectomy of a single thoracic vertebra to expose the spinal cord as described (Davalos et al., 2008). A cover glass was placed on the spinal cord tissue, and the spinal column was stabilized with Narishige STS-A spinal cord clamps and a MA-6N head-holding adaptor as described (Davalos et al., 2008). Twelve mg/kg Sulforhodamine 101 (MP Biomedicals) was intraperitoneally administered at 15 min before intravenous injection of 1 mg/kg PBB3. Intravital 2-photon fluorescence images were acquired as in the *ex vivo* assays. The detection wavelengths for PBB3 and Sulforhodamine 101 were 500 – 550 nm and 573 – 648 nm, respectively. The brain and spinal cord of these animals were sampled at 60 min, and localization of administered PBB3 was examined as in the *ex vivo* fluorescence microscopy.

In vivo non-laser near-infrared fluorescence imaging

Non-laser reflectance fluorescence imaging of living non-Tg WT and tau Tg mice was carried out using a multizoom optical system (OV100; Olympus). Mice were anesthetized with 1.5% (v/v) isoflurane. They were then given a slow bolus intravenous injection of 1 mg/kg PBB5 in 100 μl of saline containing 20%DMSO. *In vivo* fluorescence signals were generated with a mercury arc and a 620 ± 60 nm excitation filter, and the signals were detected with a 700 ± 75 nm emission filter. Following the intravital observation, brains and spinal cords were removed from these mice, and then re-examined by the same optics.

In vivo and *ex vivo* pulsed laser scanning imaging

Fluorescence was induced by 635-nm pulsed laser diode (laser power, 25-125 mW adjusted for each experiment; laser repetition rate, 80 MHz; pulse width ~ 100 ps), and emitted fluorescence was detected with a 650-nm long-pass filter and a fast-response photomultiplier tube. In the experiments, a uniform distance between the top surface of the head and the detector was achieved by fine vertical movement of the stage and a side-view camera. Mice were intravenously injected with 0.1 mg/kg PBB5 in 100 μl saline containing 20% DMSO, and their heads were scanned with a step size of 1.0 mm and time-point spread function integration time of 0.1-0.3 s (optimized for each scan) per scan point. Dynamic image acquisition was conducted over 360 min, consisting of multiple scans at baseline (before injection) and at 5, 10, 15, 30, 45, 60, 90, 120, 180, 240, 300 and 360 min after tracer injection. Fluorescence intensity was normalized among scans by laser power and integration time. ROI-based analyses were also performed in the head areas corresponding to the frontal cortex, brain stem and cervical spinal cord. Brains of these animals were dissected out after *in vivo* assays, fixed with 4% paraformaldehyde, and 20-μm frozen sections were stained with FSB and AT8 as in the *in vitro* experiments. Likewise, measurements and mapping of fluorescence intensity were carried out for brain samples homogenized with 10 volumes of PBS collected from WT and PS19 mice at 20 hr after PBB5 injection.

In vitro and *ex vivo* fluorescence microscopy for rTg4510 mouse brains

Brain sections were generated from 8-month-old rTg4510 and WT mice, and *in vitro* fluorescence staining of these sections with FSB and PBBs was performed as in

experiments for PS19 Tg mouse brain tissue. *Ex vivo* fluorescence labeling of mouse brains with PBB3 was also conducted following a protocol similar to experiments for PS19 Tg mice. *Ex vivo* tissue sections were microscopically examined with Panoramic 250 digital slide scanner (PerkinElmer).

HPLC and LC-MS analyses for the biodistribution of PBBs

Non-Tg WT mice on a C57BL/6 background at 3 months of age were intravenously injected with 1 mg/kg PBB1-4 in 200 ml saline containing 20% DMSO, and blood and brain samples were collected at 5 and 30 min after the tracer injection. Whole blood was diluted in 4 volumes of 50 mM PBS (pH 7.4), and 0.95 ml solution was mixed with 0.05-ml internal standard. The samples were then extracted by a vortex mixture with 5 volumes of ethyl acetate for 3 min. Organic and aqueous fractions were separated by centrifugation at 3,000 rpm for 15 min, and 3 ml of the organic phase was transferred to a conical tip glass tube, and was evaporated to dryness. The residues were reconstituted in HPLC mobile phase, and all reconstitutions were chromatographed on a C18 column (Inertsil ODS-3 for PBB1-3; Shodex Asahipak ODP-50 for PBB4) kept at 40°C, and were eluted with mobile phase (methanol/H_2O = 75/25 for PBB1-3; acetonitrile/0.1 M citric acid-sodium acetate buffer = 70/30 for PBB4) at a flow rate of 1 ml/min. A fluorescence detector (M-17480; Eicom) was operated at excitation and emission wavelengths of 420 and 560 nm, respectively. Similarly, blood and brain samples were obtained from WT mice at 5 and 30 min after intravenous administration of 1 mg/kg PBB5 dissolved in 200 μl saline containing 20% DMSO. Blood from 5 mice was then combined as a pooled sample. Whole blood was diluted in 4 volumes of 50 mM PBS (pH 7.4), and 0.95 ml solution was mixed with 0.05 ml internal standard (25 μg/ml

naproxen). Five brains were also homogenized in 5 ml of 50 mM PBS (pH 7.4), and 5.7 ml homogenate was mixed with 0.3 ml internal standard. The samples were then extracted by a vortex mixture with 5 volumes of ethyl acetate for 3 min. Organic and aqueous fractions were separated by centrifugation at 3,000 rpm for 15 min, and 3 ml of the organic phase was transferred to a conical tip glass tube, and evaporated to dryness. The residues were reconstituted in HPLC mobile phase, and all reconstitutions were chromatographed on a Sepax GP-C18 column (Sepax Technologies) kept at 50°C, and were eluted with mobile phase (acetonitrile/0.1 M acetic acid-ammonium acetate buffer, pH 3.5; 42/58) at a flow rate of 0.7 ml/min. Peaks corresponding to PBB5 and naproxen were detected by electrochemical detector at 1,000 mV and ultraviolet detector at 229 nm, respectively. Additionally, the standard PBB5 sample was prepared and chromatographically analyzed. Purified LC fractions of putative PBB5 metabolites were subsequently analyzed by MS (Nano LC/Linear-Trap-TOF; Hitachi).

Radiosynthesis of [^{11}C]PBB2

[^{11}C]Methyl iodide was produced from [^{11}C]carbon dioxide and converted to [^{11}C]methyl triflate, which was transferred into 500 μl of acetone containing desmethyl precursor (0.5–0.8 mg) at room temperature. After the trapping was finished, acetone was removed with nitrogen flow at 80°C and 70% acetonitrile aqueous solution (800 μl) was added to the reaction vessel. The radioactive mixture was transferred into a reservoir for HPLC purification (CAPCELL PAK C_{18} column, 10 mm × 250 mm, SHISEIDO; mobile phase, acetonitrile/water/triethylamine=700/300/1, 6 ml/min). The fraction corresponding to [^{11}C]PBB2 was collected in a flask containing 100 μl of 25% ascorbic acid solution and 75 μl of Tween 80 in 300 μl of ethanol, evaporated to dryness

under a vacuum. The residue was dissolved in 3 ml of saline (pH 7.4) for animal experiments. At the end of synthesis (EOS), [^{11}C]PBB2 (640–1340 GBq) was obtained as an injectable solution. The final formulated product was radiochemically pure (≥95%) as detected by analytic HPLC (CAPCELL PAK C_{18} column, 4.6 mm × 250 mm, SHISEIDO; acetonitrile/water/triethylamine=700/300/1, 2 ml/min). The specific activity of [^{11}C]PBB2 at EOS was 37–74 GBq/μmol, and [^{11}C]PBB2 maintained its radioactive purity exceeding 90% over 3 hr after formulation.

Radiosynthesis of [^{11}C]mPBB5

[^{11}C]Methyl iodide was produced and transferred into 300 μl of N,N-dimethylformamide containing desmethyl precursor (0.8–0.9 mg) and 0.3 mg of sodium hydride at -15°C. After the trapping was finished, the reaction mixture was heated to 80°C and maintained for 5 min. After 60% methanol aqueous solution (800 μl) was added to the reaction vessel, the radioactive mixture was transferred into a reservoir for HPLC purification (CAPCELL PAK C_{18} column, 10 mm × 250 mm; mobile phase, methanol/water/trifluoroacetic acid=600/400/0.1, 4 ml/min). The fraction corresponding to [^{11}C]mPBB5 was collected in a flask containing 100 μl of 25% ascorbic acid solution and 75 μl of Tween 80 in 300 μl of ethanol, and was evaporated to dryness under a vacuum. The residue was dissolved in 3 ml of saline (pH 7.4) to obtain [^{11}C]mPBB5 (300–560 GBq at EOS) as an injectable solution. The final formulated product was radiochemically pure (≥95%) as detected by analytic HPLC (CAPCELL PAK C_{18} column, 4.6 mm × 250 mm; methanol/water/trifluoroacetic acid=600/400/0.1, 1 ml/min). The specific activity of [^{11}C]mPBB5 at EOS was 57–74 GBq/μmol, and [^{11}C]mPBB5 maintained its radioactive purity exceeding 90% over 3 hr

after formulation.

In vitro autoradiography

Non-Tg WT and PS19 mice at 12-15 months of age were killed by decapitation, the brains were frozen, and 20-μm-thick sections were cut in a cryostat (HM560). The sections were mounted on glass slides (Matsunami Glass) and stored at -80°C pending analysis. Likewise, cortical sections were generated from brains of patients with definite AD. Tissue sections were incubated in 50 mM Tris-HCl buffer, pH 7.4, containing 20% ethanol and [^{11}C]PBB2 or 10% ethanol and [^{11}C]PBB3 (37 MBq/L, ~1 nM) at room temperature for 60 min. Nonspecific binding was determined in the presence of 10 μM nonradioactive ligands. The samples reacted with [^{11}C]PBB2 or [^{11}C]PBB3 were rinsed with ice-cold Tris-HCl buffer containing 20% or 10% ethanol, respectively, twice for 2 min, and dipped into ice-cold water for 10 sec. The slices were subsequently dried under warm blowing air and contacted to an imaging plate (Fuji Film). The imaging plate was scanned with a BAS500 system (Fuji Film) to acquire autoradiograms.

Ex vivo autoradiography

Non-Tg WT and PS19 mice at 12-15 months of age were given injections of [^{11}C]PBB2 or [^{11}C]PBB3 (~37 MBq) in the tail vein under anesthesia with 1-1.5% (v/v) isoflurane in air (2 ml/min flow rate). At 45 min after tracer administration, the mice were killed by decapitation, and brains were immediately removed and frozen in powdered dry ice. Frozen brain tissue was cut into 20-μm-thick sections by HM560 cryotome. Autoradiograms were then obtained as in the *in vitro* autoradiographic assays.

In vivo PET imaging of mice

PET scans were performed using a microPET Focus 220 animal scanner (Siemens Medical Solutions) providing 95 transaxial slices 0.851 mm (center-to-center) apart, a 19.0-cm transaxial field of view (FOV), and a 7.6-cm axial FOV (Tai et al., 2005). Prior to the scans, PS19 and non-Tg WT mice at 9 – 15 months of age were anesthetized with 1.5% (v/v) isoflurane. Emission scans were carried out for 90 min in 3D list mode with an energy window of 350-750 keV, immediately after intravenous injection of [^{11}C]PBB2 (28.3 ± 10.3 MBq), [^{11}C]PBB3 (29.7 ± 9.3 MBq) or [^{11}C]mPBB5 (32.8 ± 5.9 MBq). The radiotracer injection and following scans were conducted in a dimly lit condition to avoid photoracemization of the chemicals. All list-mode data were sorted into 3D sinograms, which were then Fourier-rebinned into 2D sinograms (frames: 10 × 1, 6 × 5, and 5 × 10 min). Summation images from 30 to 60 min and from 60 to 90 min after the tracer injection were generated with maximum a posteriori reconstruction, and dynamic images were reconstructed with filtered backprojection using a 0.5-mm Hanning's filter. VOIs were placed on multiple anatomical structures, including the brain stem and striatum, using PMOD image analysis software (PMOD Technologies) with reference to the MRI template.

In vivo PET imaging of humans

All human subjects were male, and all AD patients were diagnosed according to the National Institute of Neurological and Communicative Diseases and Stroke/Alzheimer's Disease and Related Disorders Association (NINCDS–ADRDA) criteria (McKhann et al., 1984). The Clinical Dementia Rating scale (Morris, 1993) was 0 in all of the control subjects, and ranged from 1 to 2 in the AD patients. Their cognitive functions were

assessed by MMSE (Folstein et al., 1975) (Fig. 8). None of the subjects had overt abnormalities in the brain based on MRI, apart from considerable neocortical and hippocampal atrophy in the AD patients.

PET assays were conducted with a Siemens ECAT EXACT HR+ scanner (CTI PET Systems) providing an axial FOV of 155 mm, 63 contiguous 2.46-mm-thick slices with 5.6-mm transaxial and 5.4-mm axial resolutions. A 10-min transmission scan was performed to measure tissue attenuations, and dynamic emission scan data were collected in 3-D mode over 70 min immediately after initiation of intravenous injection of [^{11}C]PIB (384 ± 83 MBq), according to a previously reported protocol (Lopresti et al., 2005) with minor modifications. Multiple frames of images (3×20 and 3×40 sec and 1×1, 2×3, 5×6 and 3×10 min) were obtained from the dynamic scan. Similarly, the second PET session with [^{11}C]PBB3 for the same individual was started approximately 2.5 hr after the end of [^{11}C]PIB-PET. [^{11}C]PBB3 (380 ± 30 MBq) was intravenously injected over 60 sec, and emission data were acquired for 70 min (frames: 3×20 and 3×40 sec and 1×1, 2×3, 5×6 and 3×10 min). During the [^{11}C]PBB3-PET scan, arterial blood samples were obtained at 10, 20, 30, 40, 50, 60, 70, 80, 90, 100 and 110 sec and 2, 2.5, 3, 4, 5, 6, 7, 8, 9, 10, 12, 15, 20, 25, 30, 40, 50, 60 and 70 min after radiotracer injection to quantify plasma radioactivities.

We defined VOIs in the cerebellar cortex, medial temporal region including the parahippocampal gyrus and hippocampus, base side of the frontal cortex, precuneus of the parietal cortex and centrum semiovale. Each VOI included three adjacent sections, and data were pooled to obtain the average radioactivity concentration for the whole VOI. SUV was calculated from time-integrated regional radioactivity concentration normalized with injected radiotracer dose per body weight. The integration interval was

30 to 70 min. Since the cerebellum could be used as a reference brain region, the SUVR to the cerebellum was determined for each target VOI as an index for plaque or tau deposition.

In addition to assays in control subjects and AD patients, PET imaging was carried out for a subject with clinical diagnosis of corticobasal syndrome. A 77-year-old female subject manifested neurological symptoms including left-side dominant muscular rigidity, dystonia, cortical sensory impairments and gait disturbance, difficulty in vertical eye movement and alien hand sign. MMSE score of this subject at the time of PET examinations was 15. Morphometric MRI indicated atrophy of bilateral frontal cortices, and right-side dominant decline of cerebral blood flow was observed by single photon emission computerized tomography with ^{99m}Tc-hexamethylpropylenamine oxime. No abnormalities related to dementia with Lewy bodies (Yoshita et al., 2006) were recognized in cardiac scintigraphy with [^{123}I]metaiodobenzylguanidine. PET imaging with [^{11}C]PBB3 and [^{11}C]PIB was performed as in the above-mentioned study for AD patients but without arterial blood sampling. Radioligand retentions were assessed by generating SUVR maps, and morphological changes were quantified on a voxel-by-voxel basis using Voxel-based Specific Regional Analysis System for Alzheimer's Disease (VSRAD) based on Statistical Parametric Mapping 8 plus diffeomorphic anatomic anatomic registration through exponentiated Lie algebra (Nakatsuka et al., 2013).

***In vitro* autoradiographic binding assays**

Sections of the hippocampus and lateral temporal cortex were generated from brains of patients with definite AD by HM560 cryotome (Carl Zeiss), and were incubated with 50

mM Tris-HCl buffer, pH 7.4, containing 10% ethanol and [^{11}C]PBB3 (approximately 1 – 1,000 pM) at room temperature for 60 min. In the homologous displacement assay, nonradioactive PBB3 (2 – 1,000 nM) was added to the buffer solution. Nonspecific radioligand binding was determined in the presence of 10 μM nonradioactive PBB3. The samples were rinsed with ice-cold Tris-HCl buffer containing 10% ethanol, twice for 2 min, and dipped into ice-cold water for 10 sec. The slices were subsequently dried under warm blowing air and contacted to an imaging plate (Fuji Film). The imaging plate was scanned with a BAS500 system (Fuji Film) to acquire autoradiograms. ROIs were defined on the hippocampal CA1 sector enriched with NFTs and gray matter of the lateral temporal cortex containing abundant senile plaques. B_{max} and K_D were calculated by non-linear hyperbolic regression against saturation plots of [^{11}C]PBB3 binding using Prism software (GraphPad).

Combined autoradiographic and histochemical analyses

In vitro autoradiography was carried out by reacting cortical sections from AD patients with [^{11}C]PBB3 (~1nM), as described in the Experimental Procedures section. Sections were thereafter stained with FSB, and different types of Aβ and tau pathologies (diffuse plaques, dense core plaques, NFTs, etc.) were localized. By matching autoradiograms and fluorescence photomicrographs, radiolabeling signals in areas enriched with each pathology were quantified to estimate amount of radioligands bound to these lesions. Rediosignal intensities were measured with Image Gauge software (Fuji Film).

Supplemental References

Berriman, J., Serpell, L. C., Oberg, K. A., Fink, A. L., Goedert, M., and Crowther, R. A. (2003) Tau filaments from human brain and from *in vitro* assembly of recombinant protein show cross-β structure. Proc. Natl. Acad. Sci. U. S. A. 100, 9034-9038.

Davalos, D., Lee, J. K., Smith, W. B., Brinkman, B., Ellisman, M. H., Zheng, B., and Akassoglou, K. (2008) Stable *in vivo* imaging of densely populated glia, axons and blood vessels in the mouse spinal cord using two-photon microscopy. J. Neurosci. Methods 169, 1-7.

Fändrich, M., and Dobson, C. M. (2002) The behaviour of polyamino acid reveals an inverse side chain effect in amyloid structure formation. EMBO J. 21, 5682-5690.

Folstein, M. F., Folstein, S. E., and McHugh, P. R. (1975) "Mini-mental state". A practical method for grading the cognitive state of patients for the clinician. J. Psychiatr. Res. 12, 189-198.

Forsberg, A., Juréus, A., Cselényi, Z., Eriksdotter, M., Freund-Levi, Y., Jeppsson, F., Swahn, B. M., Sandell, J., Julin, P., Schou, M., Andersson, J., Johnström, P., Varnäs, K., Halldin, C., Farde, L., and Svensson, S. (2013) Low background and high contrast PET imaging of amyloid-β with [^{11}C]AZD2995 and [^{11}C]AZD2184 in Alzheimer's disease patients. Eur. J. Nucl. Med. Mol. Imaging 40, 580-593.

Lopresti, B. J., Klunk, W. E., Mathis, C. A., Hoge, J. A., Ziolko, S. K., Lu, X., Meltzer, C. C., Schimmel, K., Tsopelas, N. D., DeKosky, S. T., and Price, J. C. (2005) Simplified quantification of Pittsburgh Compound B amyloid imaging PET studies: a

comparative analysis. J. Nucl. Med. 46, 1959-1972.

McKhann, G., Drachman, D., Folstein, M., Katzman, R., Price, D., and Stadlan, E. M. (1984) Clinical diagnosis of Alzheimer's disease: report of the NINCDS-ADRDA Work Group under the auspices of Department of Health and Human Services Task Force on Alzheimer's Disease. Neurology 34, 939-944.

Morris, J.C. (1993) The Clinical Dementia Rating (CDR): current version and scoring rules. Neurology 43, 2412-2414.

Nakatsuka, T., Imabayashi, E., Matsuda, H., Sakakibara, R., Inaoka, T., and Terada, H. (2013) Discrimination of dementia with Lewy bodies from Alzheimer's disease using voxel-based morphometry of white matter by statistical parametric mapping 8 plus diffeomorphic anatomic registration through exponentiated Lie algebra. Neuroradiology 55, 559-566.

Raymond, S. B., Cohen, A. D., Becker, C., Price, J., and Klunk, W. E. (2012) Anomalous PiB enhancement in the superior sagittal and transverse venous sinuses. Alzheimer. Dis. Assoc. Disord. 26, 186-190.

Skovronsky, D. M., Zhang, B., Kung, M. P., Kung, H. F., Trojanowski, J. Q., and Lee, V. M. Y. (2000) *In vivo* detection of amyloid plaques in a mouse model of Alzheimer's disease. Proc. Natl. Acad. Sci. U. S. A. 97, 7609-7614.

Silva, A. C., Lee, J. H., Aoki, I., Koretsky, A. P. (2004) Manganese-enhanced magnetic resonance imaging (MEMRI): methodological and practical considerations. NMR Biomed. 17, 532-543.

Tai, Y. C., Ruangma, A., Rowland, D., Siegel, S., Newport, D. F., Chow, P. L., and Laforest, R. (2005) Performance evaluation of the microPET focus: a third-generation microPET scanner dedicated to animal imaging. J. Nucl. Med. 46, 455-463.

Wu, C., Wang, Z., Lei, H., Zhang, W., and Duan, Y. (2007) Dual binding modes of Congo red to amyloid protofibril surface observed in molecular dynamics simulations. J. Am. Chem. Soc. 129, 1225-1232.

Yang, F., Lim, G. P., Begum, A. N., Ubeda, O. J., Simmons, M. R., Ambegaokar, S. S., Chen, P. P., Kayed, R., Glabe, C. G., Frautschy, S. A., and Cole, G. M. (2005) Curcumin inhibits formation of amyloid β oligomers and fibrils, binds plaques, and reduces amyloid *in vivo*. J. Biol. Chem. 280, 5892-5901.

Yoshita, M., Taki, J., Yokoyama, K., Noguchi-Shinohara, M., Matsumoto, Y., Nakajima, K., and Yamada, M. (2006) Value of ^{123}I-MIBG radioactivity in the differential diagnosis of DLB from AD. Neurology 66, 1850-1854.

Available online at www.sciencedirect.com

ScienceDirect

www.elsevier.com/locate/brainres

Brain Research

Research Report

Assessment of radioligands for PET imaging of cyclooxygenase-2 in an ischemic neuronal injury model

Bin Ji[a], *Katsushi Kumata*[a], *Hirotaka Onoe*[b], *Hiroyuki Kaneko*[a], *Ming-Rong Zhang*[a], *Chie Seki*[a], *Maiko Ono*[a], *Miho Shukuri*[b], *Masaki Tokunaga*[a], *Takeharu Minamihisamatsu*[a], *Tetsuya Suhara*[a], *Makoto Higuchi*[a,*]

[a]*Molecular Imaging Center, National Institute of Radiological Sciences, 4-9-1, Anagawa, Inage-ku, Chiba, Chiba 263-8555, Japan*

[b]*RIKEN Center for Molecular Imaging Science, Kobe, Hyogo, Japan*

ARTICLE INFO

Article history:
Accepted 14 August 2013

Keywords:
Autoradiography
Brain ischemia
Inflammation
Molecular imaging
Positron emission tomography (PET)
Cyclooxygenase-2 (COX-2)

ABSTRACT

Cyclooxygenase-2 (COX-2) plays crucial roles in progressive neuronal death in ischemic brain injury. In the present study, we evaluated two radiolabeled COX-2 selective inhibitors, [^{11}C]celecoxib and [^{11}C]rofecoxib, as positron emission tomography (PET) tracers for COX-2 imaging in normal and ischemic mouse brains. We also took advantage of our newly-generated antibody highly selective for mouse COX-2 to prove accumulation of the radioligands in regions enriched with COX-2. *In vitro* autoradiography demonstrated specific binding of high-concentration [^{11}C]rofecoxib but not [^{11}C]celecoxib to the cerebellum and brain stem of normal brains wherein COX-2 immunoreactivity in neurons was most abundantly observed. Meanwhile, both of these radioligands failed to detect COX-2 expression in PET assays despite their excellent brain permeability. Hypoperfusion-induced ischemia caused marked necrotic neuron death accompanied by gliosis and enhancement of neuronal COX-2 immunoreactivity in the hippocampus. Correspondingly, *in vitro* autoradiographic binding of [^{11}C]rofecoxib was increased in the injured hippocampus compared to the uninjured contralateral region, but failed in living brains of ischemia model likewise. Our work provides the rationale for monitoring COX-2 as a biomarker reflecting ischemic brain injuries and demonstrates that [^{11}C]rofecoxib, not [^{11}C]celecoxib, is useful for *in vitro* assays of COX-2, but its affinity would be insufficient for *in vivo* PET visualization.

1. Introduction

Cyclooxygenase (COX) is an enzyme that catalyzes the first two steps in the biosynthesis of prostanoids. The constitutively expressed isoform COX-1 is regarded as a housekeeping enzyme responsible for the normal production of prostanoids. The inducible isoform COX-2 is tightly regulated at transcriptional and translational levels. Under normal circumstances, few tissues express COX-2, but inflammatory cytokines and other stimuli rapidly induce the expression of COX-2 mRNA and

*Corresponding author. Fax: +81 43 253 0396.
E-mail address: mhiguchi@nirs.go.jp (M. Higuchi).

0006-8993/$ - see front matter © 2013 Elsevier B.V. All rights reserved.
http://dx.doi.org/10.1016/j.brainres.2013.08.026

protein (Candelario-Jalil and Fiebich, 2008; Collaco-Moraes et al., 1996; Minghetti, 2004; Nakayama et al., 1998). The brain is one of the few tissues constitutively expressing COX-2, which has been reported to participate in physiological control of synaptic plasticity (Kaufmann et al., 1996; Kaufmann et al., 1997). A wide body of evidence has suggested a close relationship between COX-2 and neurological disorders including cerebrovascular and neurodegenerative diseases (Candelario-Jalil and Fiebich, 2008; Minghetti, 2004; Yiangou et al., 2006). Focal cerebral ischemia, such as ischemic stroke, is a leading cause of death and adult disability in industrialized countries. A plethora of reports has shown that COX-2 expression is markedly upregulated following global or focal ischemia in experimental models, and COX-2 upregulation was also observed in postmortem brain tissues from patients who died 1–2 days following ischemic stroke (Collaco-Moraes et al., 1996; Iadecola et al., 1999; Nakayama et al., 1998; Nogawa et al., 1997). Functional ablation of COX-2 with selective inhibitors has protected neurons from global and focal ischemic injuries (Nakayama et al., 1998; Nogawa et al., 1997), indicating a critical role of COX-2 in ischemia-induced neurotoxicity. Although the neuroprotective mechanism of COX-2 inhibition has not yet been entirely clarified, COX-2-catalyzed biosynthesis of inflammatory mediators such as prostaglandins and free radical oxygen species is implicated in pathogenic events leading to progressive neuron death (Candelario-Jalil and Fiebich, 2008).

For pursuing the rapid induction of COX-2 following cerebral ischemia and its potentially critical roles in the pathogenesis of ischemic brain injury in living subjects, *in vivo* positron emission tomographic (PET) imaging of COX-2 with specific radioligands has been attempted in normal and inflammatory animal models for the last several decades, but detection of inflammation-associated COX-2 expression has not been successful (de Vries et al., 2003, 2006; McCarthy et al., 2002; Yamamoto et al., 2011). Celecoxib and rofecoxib are first-generation COX-2-selective inhibitors with high selectivity and affinity for COX-2 (Chan et al., 1999; Penning et al., 1997). Although Jaya et al. conducted *in vivo* PET imaging of rat brains with [^{18}F]celecoxib, they observed significant de[^{18}F]fluorination of the radioligand, inducing marked bone labeling (Prabhakaran et al., 2007). de Vries et al. performed *ex vivo* and *in vivo* COX-2 imaging with [^{11}C]rofecoxib. *Ex vivo* data showed specific radioligand binding to the cingulate and frontopolar cortices in normal rat brains, but demonstrated no increased signals reflecting COX-2 upregulation in two rat models of neuroinflammation (de Vries et al., 2008). It has hitherto been unclear whether difficulties in detecting inflammation-associated COX-2 expression with [^{11}C]rofecoxib were due to their insufficient affinity and/or specificity for COX-2, or due to a lack of high-level COX-2 expression in these animal models, as there were no immunohistochemical or biochemical data to confirm the induction of COX-2.

In the present study, we performed *in vitro* autoradiographic and *in vivo* PET assays of COX-2 in normal and ischemic mouse brains with [^{11}C]celecoxib and [^{11}C]rofecoxib (Fig. 1), in order to examine the feasibility of monitoring inflammatory processes in brain injuries using these radioligands. Localization and levels of COX-2 were also immunohistochemically investigated in these brains with a newly developed antibody against murine COX-2.

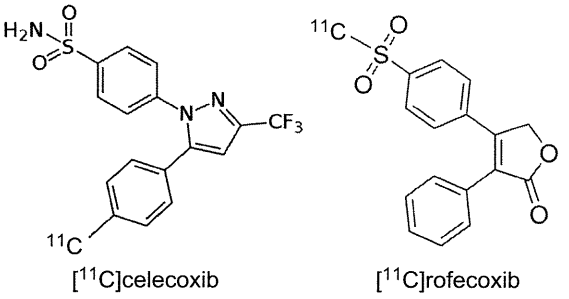

Fig. 1 – Chemical structures of [^{11}C]celecoxib and [^{11}C]rofecoxib.

2. Results

2.1. *Expression of COX-2 in normal mouse brain*

Immunohistochemical staining with our original antibody against murine COX-2 showed that most of the COX-2 expression was localized in neurons in all examined brain regions including the frontal and parietal cortices, striatum, hippocampal CA3 sector, thalamus, cerebellum and brainstem of normal wild-type mice (Fig. 2). COX-2 was most abundantly expressed in cerebellar Purkinje cells, followed by the brainstem, based on the immunofluorescence intensity. COX-2 immunoreactivity in other regions was also detectable, but was very weak compared to the cerebellum and brainstem. The absence of immunolabeling in all corresponding regions of COX-2 KO mouse brains clearly proved the specificity of our original antibody for murine COX-2 in immunohistochemical analysis (Fig. 2), while this antibody was not available for biochemical analysis, because we could not identify COX-2-specific bands in homogenates of normal mouse brains as compared to COX-2 KO mouse brain samples (data not shown).

2.2. *In vitro autoradiographic and in vivo PET analyses of normal mouse brains with [^{11}C]celecoxib and [^{11}C]rofecoxib*

In vitro autoradiographic labeling of [^{11}C]celecoxib at regular concentration (37 MBq/L) was mainly concentrated on myelin-rich regions, such as the corpus callosum, thalamus, cerebellar white matter and brainstem, and was not blocked by the addition of unlabeled celecoxib (Fig. 3A), suggesting that there was no detectable specific binding of [^{11}C]celecoxib to COX-2. A higher radioligand concentration intensified nonspecific radiolabeling but did not induce specific signals corresponding to immunohistochemical localization of COX-2 (data not shown). *In vivo* PET study demonstrated that uptake of [^{11}C]celecoxib into the brain reached a peak value of approximately 3% ID/ml at 10–15 min after bolus injection. Pretreatment with unlabeled celecoxib increased the radioligand uptake into the brain at initial phase but did not affect the retention of this tracer in the brain at 90 min (Fig. 3B, C). These results demonstrated the inability of [^{11}C]celecoxib to visualize normally expressed COX-2, primarily as a result of its high nonspecific binding and low affinity and specificity for COX-2.

Autoradiographic analysis showed that there was negligible total binding of [^{11}C]rofecoxib when brain sections were

Please cite this article as: Ji, B., et al., Assessment of radioligands for PET imaging of cyclooxygenase-2 in an ischemic neuronal injury model. Brain Research (2013), http://dx.doi.org/10.1016/j.brainres.2013.08.026

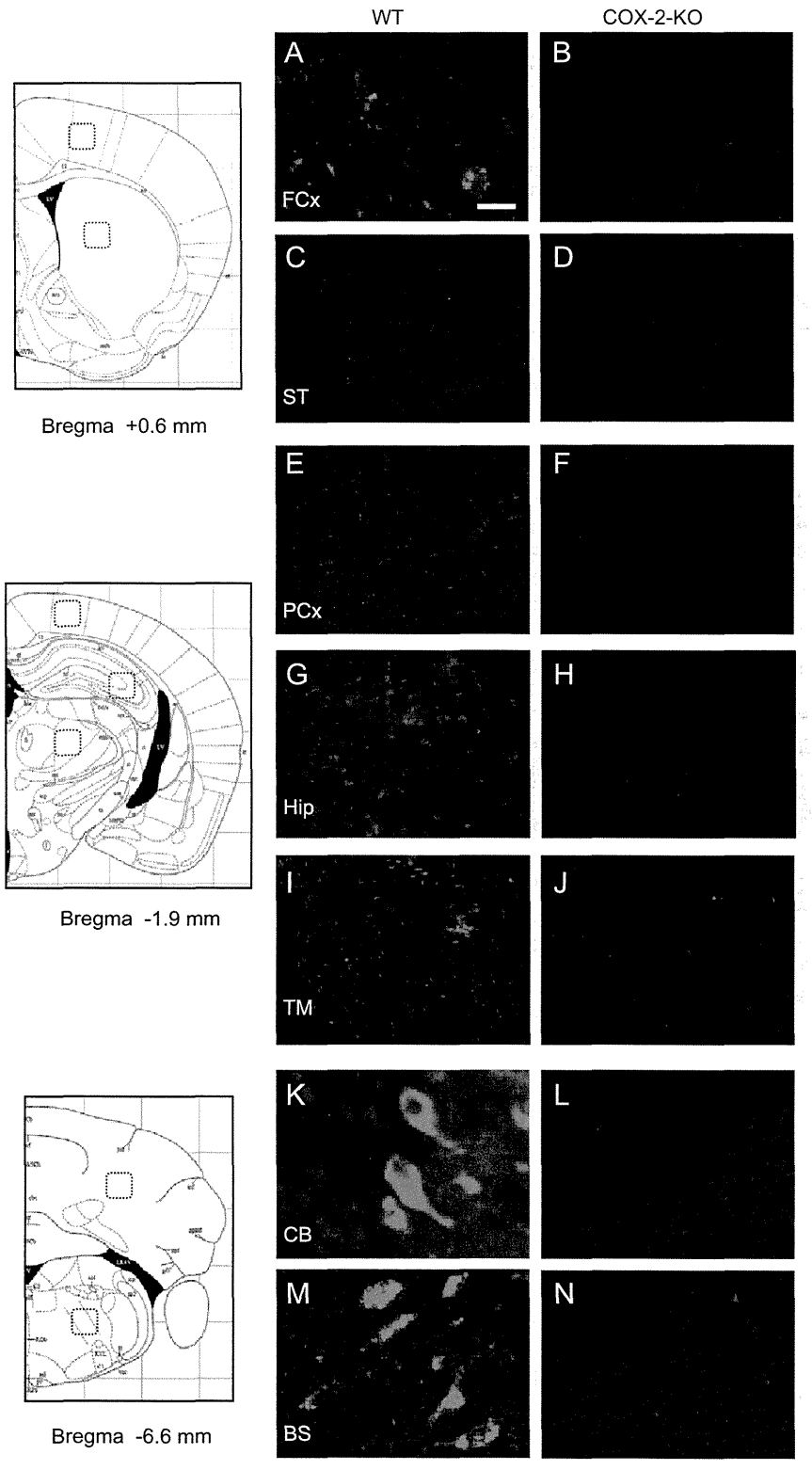

Fig. 2 – Constitutive expression of COX-2 in the brains of normal mice. Red rectangles in brain atlases (left column; from top to bottom, atlases representing coronal sections at 0.6 mm, −1.9 mm, and −6.6 mm anterior to the bregma) indicated microscopically examined areas in the frontal cortex (FCx; A and B), striatum (ST; C and D), parietal cortex (PCx; E and F), hippocampus (Hip; G and H), thalamus (TM; I and J), cerebellum (CB; K and L) and brainstem (BS; M and N) in the order from top to bottom. Immunohistochemical analysis with our original antibody against murine COX-2 showed that COX-2 immunoreactivity was present in all regions of the normal mouse brain (middle column), with the most abundant in CB (K), followed by BS (M). Immunolabeling was undetectable in the COX-2-knockout (COX-2-KO, right column) mouse brain. Scale bar: 20 μm.

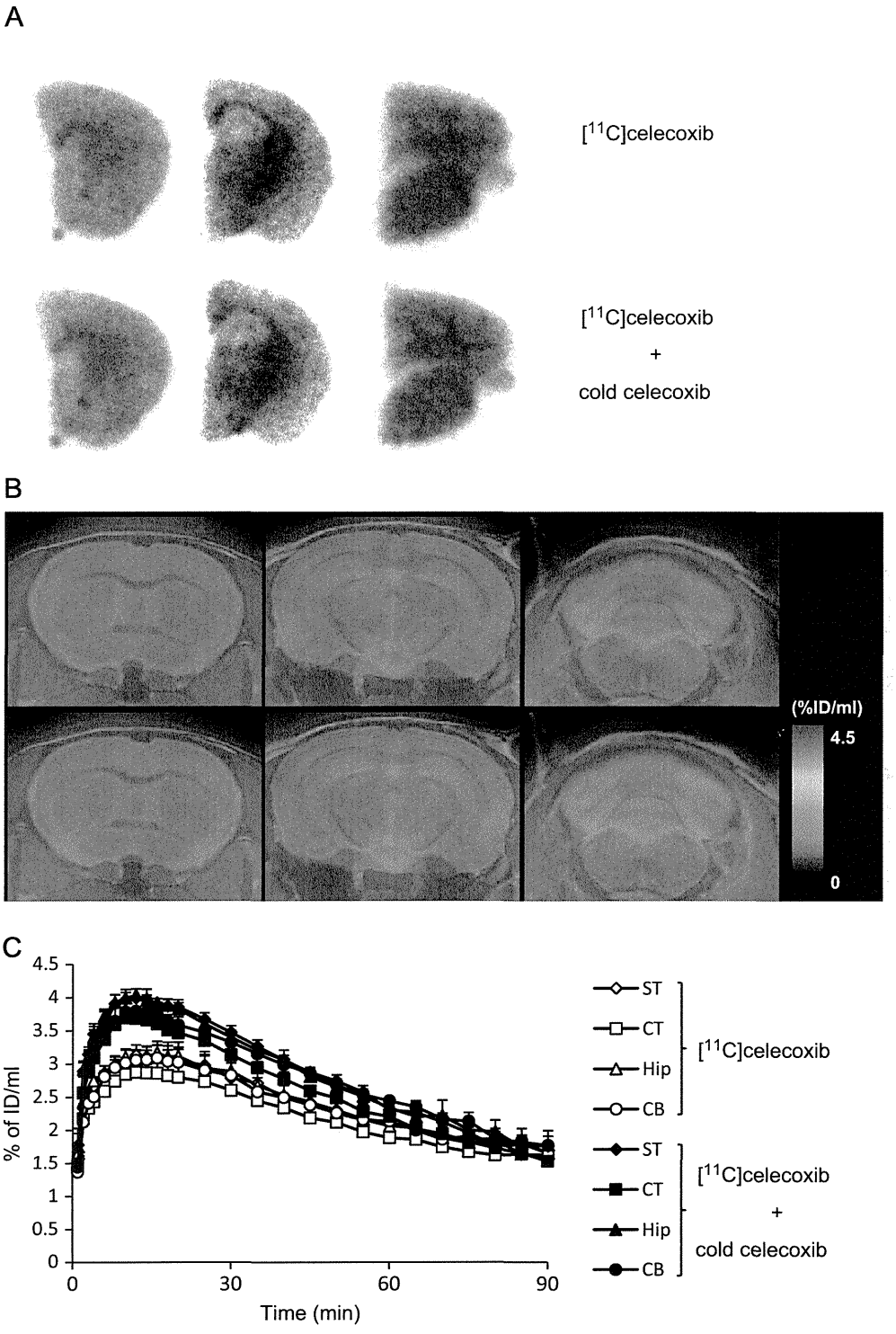

Fig. 3 – *In vitro* and *in vivo* imaging of the normal mouse brain with [^{11}C]celecoxib. (A), *In vitro* autoradiographic binding of [^{11}C] celecoxib in the normal mouse brain. (B) *In vivo* PET images generated by averaging dynamic scan data at 0–90 min after i.v. administration of [^{11}C]celecoxib without (upper panels) or with (lower panels) pretreatment of the subject with nonradiolabeled celecoxib. Images were overlaid on the MRI template. (C) Time-radioactivity curves for the striatum (ST, diamonds), neocortex (CT, rectangles), hippocampus (Hip, triangles), and cerebellum (CB, circles) in normal mice given injection of [^{11}C]celecoxib without (open symbols) or with (closed symbols) pretreatment with nonradiolabeled celecoxib (n=3~4 in each group). Vertical bars in graph denote SE. From left to right, the brain images in Panels (A) and (B) represent coronal sections at 0.6 mm, −1.9 mm, and −6.6 mm anterior to the bregma.

Please cite this article as: Ji, B., et al., Assessment of radioligands for PET imaging of cyclooxygenase-2 in an ischemic neuronal injury model. Brain Research (2013), http://dx.doi.org/10.1016/j.brainres.2013.08.026

incubated at a concentration lower than 0.37 GBq/L (approximately 10-times higher than the usual radioactivity used for auroradiography) (data not shown), while radiosignals became noticeable by increasing the radioligand concentration to 11.1 GBq/L. Under this experimental condition, the addition of unlabeled rofecoxib significantly decreased the binding of [^{11}C]rofecoxib in the cerebellum and brainstem. This distribution of the specific binding of [^{11}C]rofecoxib was consistent with the immunohistochemical observations of COX-2 (Fig. 4), suggesting that high-concentration [^{11}C]rofecoxib can be used for the *in vitro* detection of COX-2 in normal brain slices.

[^{11}C]rofecoxib showed excellent brain permeability, with a peak uptake value of approximately 5% ID/ml. It also underwent rapid washout from the brain, but there was no overt difference in radioligand retention among regions. Pretreatment of mice with unlabeled rofecoxib did not block binding of the radioligand in the brain, but rather increased its uptake and retention (Fig. 5), indicating that there was no specific binding of [^{11}C]rofecoxib detectable in living normal mouse brains. In consideration of the *in vitro* autoradiographic data, the injected dose of [^{11}C]rofecoxib in our PET assays did not provide the high concentration of free radioligand required for the visualization of specific binding sites.

2.3. *Detection of COX-2 expression induced by ischemic brain injuries*

All mice with overt ischemia-associated behavioral abnormalities ($n=3$) displayed neuronal injury to some extent, with the hippocampus being most severely affected. The *in vitro* autoradiographic analysis with [^{11}C]rofecoxib demonstrated that radioligand binding was increased in the injured hippocampus, wherein markedly enhanced COX-2 immunoreactivity and F-JadeB staining were found in neurons (Fig. 6D, H), compared to the corresponding uninjured region (Fig. 6A–C). Ischemia-induced increase of COX-2 was mainly localized in neuronal axons and somas (Fig. 6D), and double-channel immunostaining of COX-2 and NeuN, a biomarker for mature neurons, also clearly demonstrated their cellular co-localization, indicating ischemia-induced expression of COX-2 in neurons (Fig. 6E–G). Although ischemic injuries resulted in the formation of a necrotic core enriched with activated microglia and surrounded by astrocytes (Fig. 6I–L), no COX-2 immunoreactivity was observed in these activated glial cells. Additionally, *in vivo* PET imaging of ischemic mouse brains did not show increased uptake and retention of [^{11}C]rofecoxib in the infarcted area (data not shown). These data imply that [^{11}C]rofecoxib at the nanomolar concentration achievable in living brains during regular PET scans does not yield COX-2-specific signals.

3. Discussion

With the help of a newly developed antibody, we have confirmed the ischemia-induced COX-2 expression in injured hippocampal neurons. This result was consistent with previously published evidence (Collaco-Moraes et al., 1996; Miettinen et al., 1997; Planas et al., 1995) and suggested COX-2 as a potential biomarker reflecting ischemic brain injury. Pharmacological inhibition of COX-2 with selective inhibitors greatly attenuated neuronal injury after ischemia in experimental animal models (Iadecola et al., 1999; Nakayama et al., 1998; Nogawa et al., 1997; Sairanen et al., 1998), indicating the capability of COX-2-selective agents as therapeutic drugs. Long-term functional inhibition of COX, however, may alter the neurogenetic response, and this could negatively impact the endogenous repairing mechanisms involved in the enhancement of proliferation of neural progenitor cells following ischemia (Sasaki et al., 2003). COX-2 seems to play distinct roles in ischemic pathologies in a phase-dependent manner. In addition to the cardiovascular risk of chronic treatment with COX-2 inhibitors (Chaiamnuay et al., 2006), imprudent functional inhibition of COX-2 may not always be beneficial to the patients with ischemic cerebral diseases. *In vivo* imaging for COX-2 enables us to monitor, longitudinally, the progressive pathology and thereby to verify the most suitable therapeutic time window in preclinical and clinical studies.

Until now, no *in vitro* and *in vivo* studies have demonstrated the successful detection of COX-2 induction in animal models of neurological disorders with a COX-2-selective PET ligand. [^{18}F]SC58125 was the first reported COX-2-selective PET tracer, and its uptake into a murine macrophage cell line was dramatically increased under stimulation with a mixture of lipopolysaccharide and γ-interferon, with this increase being suppressible by pretreatment with nonradioactive SC58125. However, specific binding of [^{18}F]SC58125 was undetected *in vivo* in rats and nonhuman primates (McCarthy et al., 2002). Uptake of [^{18}F]desbromo-DuP-697 into the brain was blocked by pretreatment with a COX-2-selective inhibitor, NS-398 (de Vries et al., 2003), but no specific binding of this tracer was observed in the pig brain, questioning the utility and robustness of this radioligand in capturing COX-2 (de Vries, 2006). In the present study, we have reported the first evidence for *in vitro* visualization of COX-2 in the brain with a radiolabeled small-molecule compound. Specific binding of [^{11}C]rofecoxib in the cerebellum and brainstem of normal mice was proven by autoradiographic analyses, and binding in the hippocampus was significantly increased in response to ischemic brain injury. Meanwhile, we failed to detect any specific binding of [^{11}C]rofecoxib in PET imaging of living normal or ischemic mouse brains. Addition of cold compounds (non-radiolabeled celecoxib and rofecoxib) indeed increased initial brain uptake and subsequent retention of radioligands over the scan time, likely due to increased concentration of radioligands in circulation. Increase of plasma radioligand concentration can occur as a consequence of its competitively inhibited metabolism and excretion and/or displacement from specific binding site in peripheral organs in the presence of high-concentration cold ligands, and is occasionally observable in radioligand studies (Maeda et al., 2004). The rise of initial brain uptake of radioligand could hinder sensitive and precise detection of blockade of specific radioligand binding by cold compounds, and this is especially likely if *in vivo* affinity of [^{11}C] celecoxib or [^{11}C]rofecoxib for COX-2 is relatively low. Measurement of arterial plasma concentration of radioligand would provide useful information to explain why brain uptake was increased in the presence of cold compounds, and the radioligand retention in the brain in each condition would be more precisely quantified by determining volume of distribution.

Please cite this article as: Ji, B., et al., Assessment of radioligands for PET imaging of cyclooxygenase-2 in an ischemic neuronal injury model. Brain Research (2013), http://dx.doi.org/10.1016/j.brainres.2013.08.026